Experimental Mechanics (2016) 56:359–368
DOI 10.1007/s11340-015-0107-0

The Role of Surface Structure in Normal Contact Stiffness

C. Zhai[1] · Y. Gan[1] · D. Hanaor[1] · G. Proust[1] · D. Retraint[2]

Received: 15 June 2015 / Accepted: 16 October 2015 / Published online: 23 October 2015

Abstract The effects of roughness and fractality on the normal contact stiffness of rough surfaces were investigated by considering samples of isotropically roughened aluminium. Surface features of samples were altered by polishing and by five surface mechanical treatments using different sized particles. Surface topology was characterised by interferometry-based profilometry and electron microscopy. Subsequently, the normal contact stiffness was evaluated through flat-tipped diamond nanoindentation tests employing the partial unloading method to isolate elastic deformation. Three indenter tips of various sizes were utilised in order to gain results across a wide range of stress levels. We focus on establishing relationships between interfacial stiffness and roughness descriptors, combined with the effects of the fractal dimension of surfaces over various length scales. The experimental results show that the observed contact stiffness is a power-law function of the normal force with the exponent of this relationship closely correlated to surfaces' values of fractal dimension, yielding corresponding correlation coefficients above 90 %. A relatively weak correlation coefficient of 60 % was found between the exponent and surfaces' RMS roughness values. The RMS roughness mainly contributes to the magnitude of the contact stiffness, when surfaces have similar fractal structures at a given loading, with a correlation coefficient of −95 %. These findings from this work can be served as the experimental basis for modelling contact stiffness on various rough surfaces.

Keywords Contact mechanics · Contact stiffness · Rough surfaces · Fractal dimension · Nanoindentation

Introduction

In contact mechanics, surface morphology plays an essential role in determining how solids interact with one another, with significance in many processes including friction, wear, thermal and electrical conduction [1–3]. The classic Hertzian contact theory considers elastic solids with smooth profiles of curved surfaces connecting the applied force and indentation depth, by assuming a distribution of normal pressure in the contact area. However, this assumption neglects topological features of natural surfaces and the interaction between individual contact regions [2]. The existence of surface roughness results in only a certain number of peaks or asperities being in contact. Since the true contact area at an individual asperity can be of nanoscale dimensions, the real contact area between two surfaces is typically orders of magnitude smaller than the apparent or nominal contact area. As early as the 1950s, Bowden and Tabor had already recognized the significance of the surface roughness of contacting bodies in contact mechanics. Since then, the mechanics of rough interfaces have been broadly studied on the basis of early contributions by Archard [4] and Greenwood and Williamson [5]. In the past few years, many studies have been carried out to interpret parameters of contact area and normal contact stiffness under various loading forces, for different surface characteristics [6–9]. It has been theoretically and numerically found that in non-adhesive contact, the contact area between rough elastic surfaces depends linearly on the normal force and is inversely

✉ C. Zhai
c.zhai@sydney.edu.au

[1] School of Civil Engineering, The University of Sydney, Sydney, NSW 2006, Australia

[2] ICD-Lasmis, Université de Technologie de Troyes (UTT), CNRS UMR 6279, 12 Rue Marie Curie, 10010 Troyes, France

proportional to elastic modulus and the root mean square (RMS) slope of the surface [10–12].

The true interfacial contact area along with roughness parameters could, at some level, be utilised to interpret the mechanics of rough surfaces subjected to an applied normal load [13, 14]. However, the determination of the real contact area between contacting bodies through experimental measurement is challenging because most natural surfaces exhibit features across a wide range of length scales [15, 16]. Rough surfaces possess complex morphologies and geometries that are difficult to quantify definitively.

Numerical analyses, using molecular dynamics, boundary element methods, etc., have been conducted and generally support the proportionality between normal force and contact stiffness, as was first mentioned in the Greenwood-Williamson model [5, 8, 10, 17]. However, other studies have reported that, for small to medium loads, the logarithm of stiffness exhibits close proportionality to the logarithm of the applied normal force, i.e. the contact stiffness k is a power function of the normal force F_N: $k \propto F_N^{\alpha}$, which differs from the prediction of Greenwood-Williamson model and the work mentioned above. This issue has been the subject of controversy and discussion in the field of contact mechanics for some years [7, 18–21].

Several related experiments have been conducted on multiscale rough surfaces to gain information pertaining to interfacial behaviour. Buzio et al. [22] employed atomic force microscopy (AFM) to explore the role of surface morphology in contact mechanics at the nanoscale. This approach was selected owing to its high sensitivity with respect to vertical displacements and normal loads. However, observations of morphological effects with nanometric tips (for example, sharp AFM tips) are encumbered by technical difficulties, e.g., uncontrolled long-range adhesive forces dominate incipient contact while adsorbed water and contaminants may smooth atomic corrugation [23, 24]. The digital image correlation and ultrasound techniques have been employed to measure the contact stiffness of real engineering interfaces, revealing that contact stiffness depends upon three main factors: contact pressure, surface roughness, and surface hardness [25]. Relationships between hierarchical surface structures, loading conditions and contact mechanics have been studied experimentally and computationally using a variety of other macroscopic approaches and a range of materials [21, 26–32]. However, significant difficulties remain in relating parameters of contact stiffness to surface structure descriptors.

The surface morphology of materials is known to be of fundamental importance in governing physical properties and interfacial phenomena. Consequently, there exists an ever increasing number of experimental techniques for the two and three dimensional characterisation of rough surfaces along with a broad range of numerical descriptors to quantify these structures using parameters such as roughness, skewness, kurtosis, curvature, slope, and fractal dimension. Among these surface descriptors, the RMS roughness, RMS slope and fractal dimension are of considerable value in comparative analysis and quantitative characterisation of surface structures. The RMS slope is commonly chosen as a higher order surface descriptor, which can be used to interpret surface phenomena. For example, optical and tribological properties at rough interfaces have been varyingly correlated with RMS slope [33, 34]. Moreover, the fractal dimension of surfaces is considered to be an important descriptor useful in representing realistic three-dimensional surface features over a wide range of length scales [35, 36]. The fractal dimension, a cross-scale surface descriptor that incorporates localised and macroscopic morphological surface behaviour, has been attracting increasing attention in the characterisation of surfaces and particles across a wide range of fields including stereology, powder technology, geology, metallurgy, and computer vision [37, 38]. The advantage of using surface fractality as a cross-scale descriptor stems partly from the tendency of first-order descriptors (e.g. RMS roughness) to be dominated by the highest scale features, while secondary descriptors (e.g. RMS slope) tend to be dominated by the finest scale surface characteristics.

In spite of the significant progress that has been made in nanoindentation and surface morphology characterisation, which facilitate the mechanical and morphological analysis of surfaces at micrometre and nanometre scales, the existing experimental results of the structure-dependence of contact behaviour of surfaces with random multiscale features are limited. In this work, we employed flat tip nanoindentation to directly observe normal contact mechanics at rough surfaces and, in conjunction with 3D profilometry, established relationships between hierarchical surface structures and exhibited contact stiffness.

Method

Sample Preparation and Characterisation

In this paper, we considered round disk samples made of aluminium alloy 5005 owing to this material's suitable chemical stability and deformability. Three surface treatment methods were applied: (1) polishing, (2) abrasive blasting and (3) surface mechanical attrition treatment (SMAT). Because the aluminium alloy used is relatively soft and ductile, the surfaces of these samples can be efficiently modified through standard polishing treatment, bead blasting and SMAT procedures. Samples with polished surfaces were prepared using sequential grinding and polishing steps with final polishing using 1 μm diamond suspension. The other two methods employed here accomplish physical modification of the surface details at different length scales depending on the size of the particles

used in the treatment. Both treatments utilised the impact of high-speed particles on specimen surfaces. Specifically, the operation of bead blasting is propelling forcibly a stream of fine glass beads to impact and modify the surface morphology. The average sizes of the two selected groups of glass beads used in the blasting treatment of the polished surfaces were 50 and 300 μm, respectively. SMAT alters surface features using an excitation mechanism to accelerate smooth steel balls and project them on the prepared sample surfaces. The surface treatments employed will introduce changes in the surface-localized microstructure, and thus may alter the material hardness. However, the material elasticity will not be strongly affected by the surface treatments, e.g. SMAT [39–42]. In our work we used three different SMAT processes using 1, 2 and 3 mm diameter balls, respectively. Figure 1 compares the samples achieved through the different methods, using a scanning electron microscope (SEM, Zeiss ULTRA plus), at the identical magnification. It can be seen clearly that samples after blasting treatment using glass beads of 50 μm present more complex and rougher texture.

To further quantitatively analyse the surface morphology, the treated aluminium surfaces were scanned using an optical surface profilometer (NanoMap 1000WLI). A standard 1024×1024 topographical imaging procedure with a vertical scanning range of 20 μm was applied with a green LED light source (with a wavelength of ~500 nm) to obtain three-dimensional topographical maps of the specimen surfaces. Subsequently, surface roughness parameters were determined from the digitised surface data across multiple scans of 1× 1 mm^2 for each individual sample. The sample surfaces were primarily characterised through two roughness descriptors, RMS roughness and RMS slope, which are two widely used surface descriptors for the characterisation of rough interfaces.

For the purpose of quantifying and comparing the prepared surfaces across a wide range of length scales, a grid of unit dimension L is superimposed in order to mesh the obtained digitised surface into a number of triangles. The variance of surface areas of different samples was calculated at different digital resolutions of the scans, as shown in Fig. 2. For example, when $L=X/4$ with X being the total scan length, the surface is covered by 32 triangles of different areas inclined at various angles with respect to the projected plane. The areas of

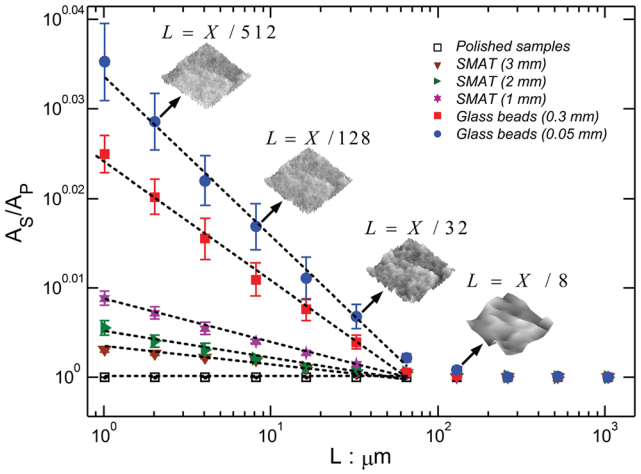

Fig. 2 The calculated sample surface areas at different scales. The insets show the digitised scans used to calculate the surface area for the samples that underwent sand blasting using 50 μm-sized glass beads

all triangles are calculated and summed to obtain a total surface area A_S for a given value of L. These triangular elements have an equal projected triangle area, although their real areas are different and the total surface area A_S is larger than the projected area of the scanned sample A_p. The grid size is then decreased by a successive factor of 2, and the previously mentioned process continues until L corresponds to the distance between two adjacent pixel points, i.e., the highest resolution of the digitised data, which is 1 μm for the optical profilometer employed in the present work. For all of the six sample surfaces, the obtained surface areas A_S at various L values exhibit an increasing trend as the grid is made finer with a smaller value of L. Of the six types of surfaces, the surface area of the sample blasted by glass beads shows more evident variation at different scales than that of the SMAT prepared samples or polished specimen. A power law relationship is found between the calculated surface area and the length resolution of digitised scan, in the range from 1 to 1000 μm. In other words, the sample surface structures exhibit self-affinity over a certain range of length scales, which can be characterised by the surfaces' fractal dimension.

In this paper, the concept of fractal dimension provides a useful method for representing rough surfaces in terms of cross-scales analysis. A number of existing algorithms have

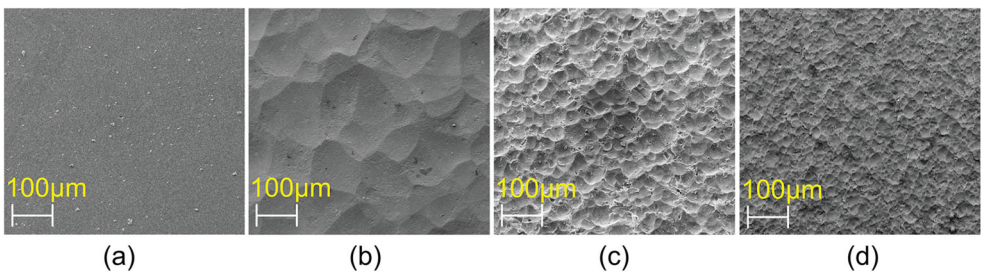

Fig. 1 SEM images of aluminium samples with different surface treatments: (**a**) polishing treatment; (**b**) SMAT using 2 mm-sized steel balls; (**c**) blasted with 300 μm-sized glass beads; (**d**) blasted with 50 μm-sized glass beads

been fully developed to determine surface fractal dimension from digitised surface data [38, 43]. Here, we used two methods to obtain the fractal dimension: (1) Scaled triangulation; (2) Cube counting. The process of the triangulation method based on cross-scale comparison is illustrated in Fig. 2, demonstrating the calculated surface areas at various scales. The error bars are achieved over five samples for each type of surface. The box-counting approach is also applied here as a comparison [44, 45]. For both methods, an anisotropic scaling is applied to normalise three-dimensional scans, making both methods suitable to self-affine surfaces.

As shown in Table 1, six typical surface types with distinct surface details were prepared and characterised prior to nanoindentation tests. For each surface type, the mean values of roughness descriptors were obtained over ten scans and the corresponding standard deviations showed these surface measures were representative. The resulting values are reported as indicated in Table 1 including the mean RMS roughness, RMS slope, and fractal dimension. The two calculation methods used here to obtain the values of fractal dimension are principally in agreement with each other, with the values of fractal dimension inverse to the sizes of particles applied in SMAT and glass-bead blasting treatments. Moreover, the RMS slope and fractal dimension obtained from both methods show similar trends, i.e., smaller particles used to modify the surfaces lead to larger RMS slope and fractal dimension values. As for the RMS roughness, results show that the parameter has no clear correlation with varying particle sizes.

Contact Stiffness Measurement Using Nanoindentation

Surface contact stiffness of aluminium samples with different surface morphology was analysed by means of nanoindentation tests with three flat indenter tips with different diameter sizes: 54.1, 108.7, and 502.6 μm (SYNTON-MDP, FLT-D050, FLT-D100, and FLT-D500), as shown in Fig. 3. The tips have sizes comparable with the size of the particles used to modify the surface of the specimens and the roll-off wavelength found in the power spectra of the surfaces ranging from 50 to 250 μm [43]. The three flat indenter tips were also examined by profilometery, and were found to exhibit an average RMS roughness of less than 0.04 μm, and thus in the following calculations, the tip surfaces were assumed to be ideally smooth. The reason for choosing flat tips is that the apparent contact area under the tip does not change with respect to the indentation depth, which is not the case for spherical or Berkovich tips. All the tips and specimens under tests were properly cleaned using water and compressed air to remove any embedded grains and particles. Cleaning with ethanol and heat treatment (around 120 °C) were also applied to remove surface contamination and physisorbed moisture. When the flat indenter tip first contacts the sample surface, the actual contact area is only a small fraction of the nominal contact area. The asperities of the sample surface at contact regions are squeezed against the flat tip, deforming elastically or plastically. For the purpose of evaluating only the elastic responses, 10 partial unloading procedures were employed by decreasing the applied load by 10 %, in the course of each individual test. After each unloading stage, the loading level rose by a factor of two to the next unloading stage, until the load reached 500 mN where the last unloading was performed. All the values of stiffness were determined by averaging over 10 indentation tests at different positions on each surface type. Analogous analytical procedures have been implemented experimentally at aluminium interfaces in the past using a method of ultrasonic loading [46] and computationally in the framework of finite element analyses [47]. The unloading stiffness k (in units of N/m) was defined as the slope of the unloading curve, $k=\mathrm{d}P/\mathrm{d}S$, where P designates the load and S is the indentation depth, as indicated in Fig. 3. Subsequently, the reduced elastic modulus E_r can be derived from the measured unloading stiffness through the relation:

$$E_r = \frac{\sqrt{\pi}}{2}\frac{k}{\sqrt{A}}, \tag{1}$$

where A is the nominal contact area of the indenter tip. Equation (1) is a fundamental equation for assessing the elastic properties in nanoidentation tests, and has been shown to be equally applicable in cases of elastic–plastic contact [48–51]. The applicability of this formula when plastic deformation

Table 1 Sample surface characterisation with different treatments

Surface treatment	RMS Roughness R_{RMS}/ μm	RMS slope R_S	Fractal dimension D_{f1} / Triangulation	Fractal dimension D_{f2} / Cube counting
1. Polish	0.05712±0.005431	0.009101±0.0009640	2.093±0.06176	2.024±0.04101
2. SMAT3mm Particle size: 3 mm	4.012±0.3674	0.08280±0.007314	2.185±0.0351	2.149±0.02543
3. SMAT2mm Particle size: 2 mm	2.730±0.2554	0.07633±0.00397	2.228±0.01987	2.156±0.01308
4. SMAT1mm Particle size: 1 mm	1.152±0.3124	0.04864±0.01137	2.337±0.01818	2.233±0.01659
5. GB300 μm Blasted by glass beads of 300 μm	4.179±0.1943	0.2244±0.01537	2.551±0.02170	2.424±0.02572
6. GB50 μm Blasted by glass beads of 50 μm	2.970±0.2759	0.2023±0.01022	2.626±0.01736	2.351±0.03633

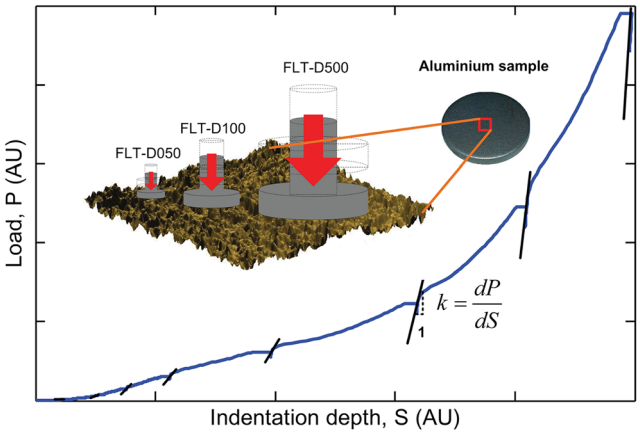

Fig. 3 Typical loading-displacement curve of nanoindentation tests on the sample surfaces, in arbitrary units (AU). Partial unloading processes were applied to isolate elastic contributions to contact stiffness under different loading levels. Three flat indenter tips used in the experiments (FLT-D050, FLT-D100, FLT-D500) are also illustrated for comparison

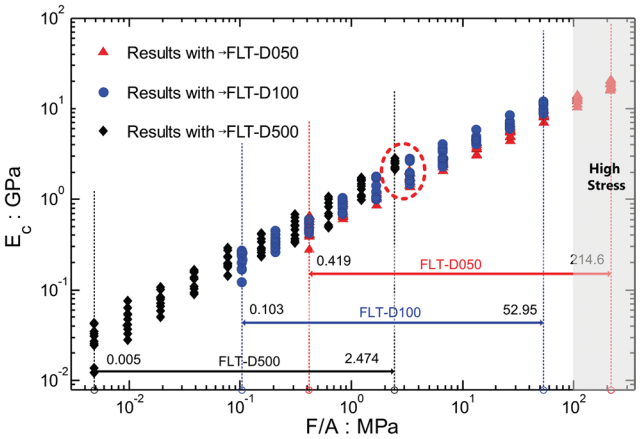

Fig. 4 Contact stiffness, E_C, measured from rough surfaces with sand blasting treatment of glass beads of 50 μm diameter (GB50μm). Raw data are from multiple indentation tests at different loading levels, F/A, where F is the normal force and A denotes the projected area of the flat tip

occurs during the indentation experiments has been the subject of numerous studies [52, 53].

Considering the fact that the measured reduced elastic modulus E_r includes contributions from both the tested specimen and the indenter tip, the contact stiffness, E_c (in the unit of N/m^2), is estimated from

$$\frac{1}{E_r} = \frac{1-\nu_c^2}{E_c} + \frac{1-\nu_i^2}{E_i}, \tag{2}$$

where the subscript i indicates the property of the indenter tip material, the subscript c the properties of the tested specimen and υ is the material's Poisson's ratio. For the diamond indenter tips used in this research, E_i and ν_i are typically 1140 GPa and 0.07, respectively. For the aluminium samples employed here, ν_c is set as 0.3.

Results and Discussion

Experimental Data

Figure 4 presents the typical measured contact stiffness of rough surfaces created by sand blasting treatment with 50 μm diameter glass beads (Sample GB50μm) obtained from nanoindentation tests with three tips of different sizes. The stress was calculated from the ratio of loading force to the projected area of the indenter tips. Figure 4 shows that, by using different sized tips, the stress range extends over several orders of magnitude. With the same maximum force (~500 mN) provided by the nanoindenter, the maximum stress produced with FLT-D050 was around 100 times larger than that of the FLT-D500. The stress provided by all the three indenter tips ranged from 0.005 to 214.6 MPa, crossing five orders of magnitude with the FLT-D500, FLT-D100, FLT-D050 corresponding to the ranges (shown in Fig. 4) of 0.05 to 2.474 MPa, 0.103 to 52.95 MPa, and 0.419 to 214.6 MPa, respectively. The contact stiffness measured over this range of applied stresses varies approximately from 0.01 to 55 GPa.

It can be seen clearly that the measured contact stiffness increases with the loading force, for all tested samples, as shown in Fig. 5. Although, as mentioned in the introduction to the present work, it is the subject of some controversy, the contact stiffness has been predicted by certain reports to exhibit a power-law relation with the applied normal force, which can be described as $E_c \propto F_N^{\alpha}$, where F_N is the normal force applied on the surface and α is the exponent of the power function [13, 19, 21, 22]. At the same applied stress level, the surfaces after SMAT (Sample 2–4) or sand blasting treatment (Sample 5–6) show a smaller value of contact stiffness with respect to that of the polished surface (Sample 1). The surface blasted with glass beads of 50 μm diameter (Sample 6)

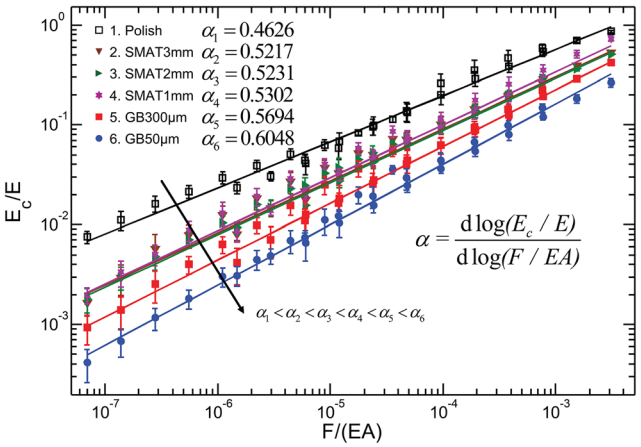

Fig. 5 Curve fitting for the normalised stiffness, E_C/E, and normalised applied load, $F/(EA)$, for six tested surfaces, with E being the Young's modulus of the tested material, and A the apparent contact area

presents the lowest contact stiffness of all the six types of surfaces. It is also found that the surfaces with the highest values of RMS slope and fractal dimension exhibit comparatively lower contact stiffness in the range of applied stress levels.

As the loading force increases towards the high stress regimes, the slope of the measured contact stiffness decreases. The trend is more pronounced as the normal stress approaches the bulk compressive strength of the aluminium alloy (shown in Fig. 4). This trend matches the expectation that with deformation of individual asperities the contact stiffness will converge to a stable value, close to the elastic stiffness of the bulk material.

For each surface, the measured contact stiffness obtained through one indenter tip briefly coincides with that of the other two indenter tips of different sizes in the overlapping stress ranges. However, compared to the results with smaller tips, the measured contact stiffness obtained with larger indenter tip (FLT-D500) tends to be larger at similar stress levels. A typical example is shown in the red dashed circle in Fig. 4. The measured contact stiffness at the maximum stress for FLT-D500 is evidently larger than the result achieved with FLT-D050 under a similar stress level. The indentation of a single asperity or fewer asperities, the likely result of the use of the 50 μm tip, occurs with lower apparent stiffness owing to the presence of unconstrained neighbouring surface features. While the exact nature of deformation mechanisms differs between materials it is likely that this phenomenon occurs to varying extents across a broad range of systems.

An alternative explanation to the increased stiffness observed with the use of larger indenter sizes is the adhesion forces between the tip and the rough surface, which are strongly affected by the true contact area. A larger tip tends to yield a relatively higher level of adhesion, resulting in higher bond strength and larger apparent contact stiffness. The adhesive force can be observed even in the absence of capillary bridges if the surfaces are sufficiently smooth [2, 54]. An estimation of bond strength can be made at the instant of surface separation at the end of the indentation tests, found typically within the range of 10 MPa [55, 56]. In our situation, an adhesive interaction between the indenter tip and the testing specimen could not be eliminated even after proper cleaning and drying processes, and it can potentially impact the measurements, particularly for cases of polished samples subjected to high applied loading forces.

Another factor that is likely to influence the measured contact stiffness in nanoindentation experiments is the oxide layer on the surfaces of aluminium samples. Aluminium alloys ubiquitously exhibit a thin passivated oxide layer arising from reaction with atmospheric oxygen. This nanoscale oxide layer exhibits locally divergent mechanical properties in a region of thickness typically less than 10 nm [57, 58]. In this research, the penetration depth of the nanoindentation test ranges from 1000 to 5000 nm. The smallest depth is observed in one test accomplished with FLT-D500 on a polished sample, where 1025.6 nm is achieved with 500 mN being the maximum force. The influence of the oxide layer is thus expected to be of limited significance owing to the considerable difference in the thickness of the oxide layer and indentation penetration depth.

To compare the contact stiffness of different surfaces, we converted the obtained values for contact elastic modulus E_c through equations (1) and (2) to non-dimensional values E_c/E by dividing the value of the Young's Modulus of aluminium alloy 5005, E=69.5 GPa. The non-dimensional stress is defined as $F/(EA)$, where A is the projected area of the corresponding tip. Note that the fitting curves are achieved, excluding the contributions from the measured stiffness under stress levels higher than 100 MPa, where the surface shows an apparent yield phenomenon. The slope α of the fitting curve can be defined as the exponent of the power function between the normalised contact modulus and normalised stress. For all the six sample surfaces, the value of the exponent α varies from 0.4626 to 0.6048, changing as the fractal dimension and the RMS slope increase. As a comparison, this typical value in cases of Hertzian contact of two elastic spheres is 1/3. The power-law relationship found here experimentally is in good agreement with previous theoretical predictions on a quantitative basis [13, 18, 19, 21].

Correlation Analysis

From the normalised data shown in Fig. 5 the relation between the contact modulus E_c and applied loading force F can be described as

$$\frac{E_c}{E} = \beta\left(\frac{F}{EA}\right)^{\alpha}. \tag{3}$$

The exponent α and amplitude β are assumed to be constant for a given surface structure. Using this form, we can obtain a set of coefficients, α and β, corresponding to the tested surfaces from the measurements in Fig. 5.

Correlations between the exponent α and the evaluated surface parameters are described in Fig. 6, where, for all tested surfaces, the exponent α is plotted against the aforementioned surface descriptors, i.e., (1) RMS roughness; (2) RMS slope; (3) fractal dimension found from a triangulation method, and (4) fractal dimension found using a box counting method. Specifically, the exponent α achieved across a wide range of stress values illustrates a relatively weak correlation to values of RMS surface roughness. While in contrast, this exponent correlates more closely to values of the fractal dimension with the corresponding correlation coefficients above 90 %. In Fig. 6(b), a correlation coefficient of around 90 % has also been found with the RMS slope, but the exponent α of the

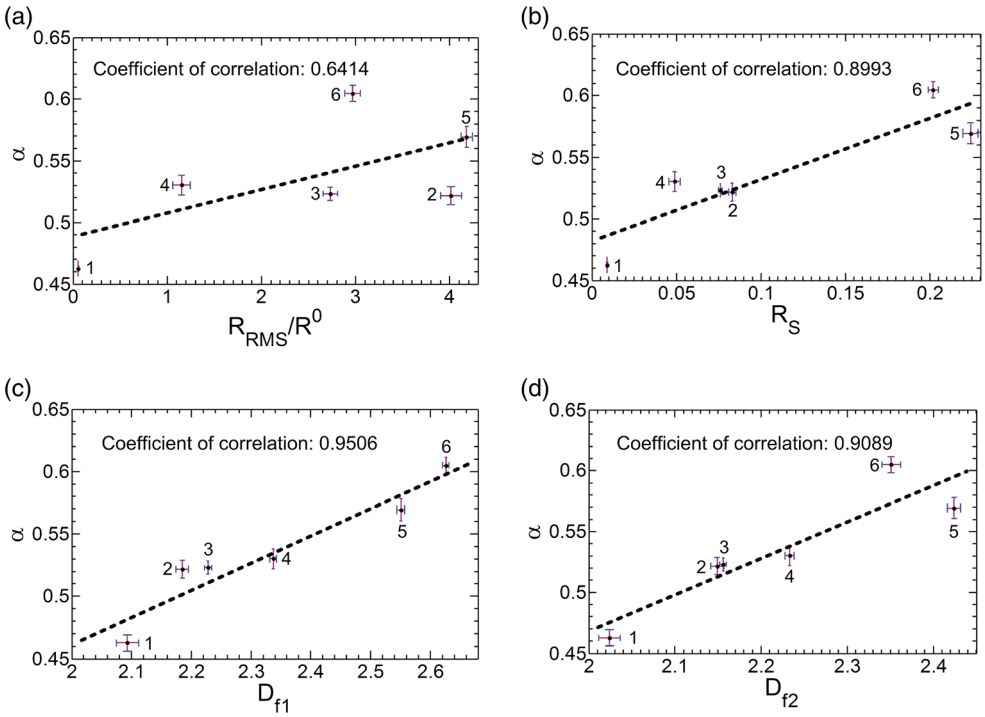

Fig. 6 Correlations between the stiffness variation exponent α and roughness parameters: (**a**) Non-dimensionalised RMS roughness R_{RMS}/R^0, with R^0=1 μm; (**b**) RMS slope; (**c**) Fractal dimension obtained with the scaled triangulation method; (**d**) Fractal dimension obtained with the cube counting method. Horizontal and vertical error bars show the corresponding standard deviations from the surface measurement and curve fitting. The sample number shown in the figures can be referred to Table 1

SMAT samples yields similar values and does not show strong correlation to the RMS slope. This, to a certain degree, is supported by numerical investigations of these descriptors reported in the literature, which, it should be noted, focused mainly on the evolution of contact area and surface separation rather than stiffness [59].

Figure 7 illustrates the significance of RMS roughness, RMS slope and fractal dimension in governing the coefficient β for the contact stiffness measured with flat tipped diamond indenters. It is found that the RMS roughness dominates β with the coefficient of correlation being −95 %, whilst the RMS slope and the fractal dimension are not as well correlated

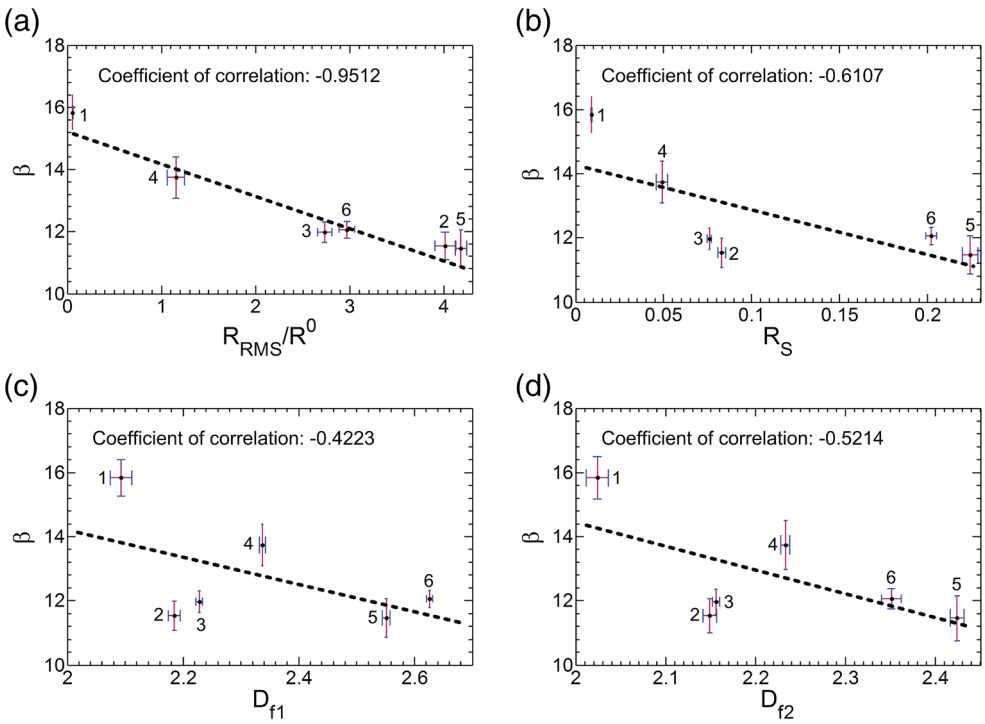

Fig. 7 Correlations between the coefficient β and roughness parameters: (**a**) Non-dimensionalised RMS roughness R_{RMS}/R^0, with R^0 being 1 μm; (**b**) RMS slope; (**c**) Fractal dimension obtained with the scaled triangulation method; (**d**) Fractal dimension obtained with the cube counting method. Horizontal and vertical error bars show the corresponding standard deviations from the surface measurement and curve fitting. The sample number shown in the figures can be referred to Table 1

Table 2 Correlations between the stiffness parameters and surface roughness parameters

	RMS Roughness $R^*=R_{RMS}$/ 1 μm	RMS slope R_S	Fractal dimension D_{f1} Triangulation	Fractal dimension D_{f2} Cube counting
α	$\alpha=0.019R^*+0.487$	$\alpha=0.503R_S+0.481$	$\alpha=0.217D_{f1}+0.029$	$\alpha=0.301D_{f2}+0.133$
β	$\beta=-1.02R^*+15.3$	$\beta=-14.1R_S+14.27$	$\beta=-4.28D_{f1}+22.8$	$\beta=-7.61D_{f2}+29.7$

with this coefficient. The RMS roughness is a parameter indicating primarily the vertical scale of the rough surface. If all the tested surface structures, along with indentation depths, were to be stretched or compressed by a selected factor yielding identical roughness ranges and the same value of β, the contact behaviour would be mainly controlled by the fractality of the surface as described by the value of its fractal dimension. The fitting functions for the stiffness parameters, i.e., α and β, using surface roughness parameters, including RMS roughness, RMS slope and fractal dimension are detailed in Table 2.

Similar formulas have been used as the theoretical approximation for the contact stiffness from Pohrt and Popov [19], Jiang et al. [21] and Komvopoulos and Ye [7]. In all the aforementioned theories, the relationship between the stiffness and pressure was found to follow a power law, with the exponent strongly correlated to the value of fractal dimension. Pohrt and Popov [19] established a power law based on boundary element simulations for a rigid square indenter over a range of normal loads spanning four orders of magnitude, concluding that the contact stiffness for low to medium loading conditions is most appropriately approximated by a power-law dependence with the exponent ranging from 0.51 to 0.77, corresponding to a variation of fractal dimension from 2 to 3 [19]. It is worth noting that the approximated value of the exponent α is $0.2567D_f$, which is rather close to the value of $0.2168D_{f1}$ found experimentally in the current work. Additionally, Jiang et al. [21] have presented a fractal model which can be applied to analyse the contact stiffness of machined plane joint surfaces, in which the exponent α of the power law is described as $D_f/(3-D_f)$. Under a given load, smaller values of both surface roughness and fractal dimension can increase the true contact area, thereby resulting in a larger number of micro-contacts yielding elastic deformation, which, in turn, increases the normal and tangential contact stiffness.

Conclusions

In this work, the effects of surface roughness and fractality on the normal contact stiffness were experimentally demonstrated for various rough surfaces. A wide range of applied stress across five orders of magnitude is achieved using three flat indenter tips of various sizes. The results in our experiments show that the contact stiffness follows a power-law function with respect to the normal force, with the exponent of this relationship ranging from 0.4626 to 0.6048, corresponding to the polished surface and the surface treated with the finest beads. This relationship is then described through an expression with two parameters, simplified as $E_c/E=\beta[F/(EA)]^{\alpha}$. Through correlation analyses, we connected the experimentally obtained coefficients, i.e., the exponent α and amplitude β, to the characterisation of rough surfaces. For a given material, the exponent α of this power law relation shows strong dependence on values of fractal dimension and RMS slope, while the coefficient β is dominated by RMS roughness. These strong correlations can be used for establishing and validating predictive models for contact stiffness on a wide range of rough surfaces.

Acknowledgments Financial support for this research from the Australian Research Council through grants DE130101639 and Civil Engineering Research Development Scheme (CERDS) in School of Civil Engineering at The University of Sydney is greatly appreciated. The authors acknowledge the facilities and the scientific and technical assistance of the Australian Microscopy & Microanalysis Research Facility at the Australian Centre for Microscopy & Microanalysis at the University of Sydney where the SEM images were taken.

References

1. Popov VL (2010) Contact mechanics and friction. Springer Science & Business Media, Berlin
2. Persson BNJ (2006) Contact mechanics for randomly rough surfaces. Surf Sci Rep 61(4):201–227
3. Assender H, Bliznyuk V, Porfyrakis K (2002) How surface topography relates to materials' properties. Science 297(5583):973–976
4. Archard J (1957) Elastic deformation and the laws of friction. Proc R Soc Lond Ser A Math Phys Sci 243(1233):190–205
5. Greenwood J, Williamson J (1966) Contact of nominally flat surfaces. Proc R Soc Lond Ser A Math Phys Sci 295(1442):300–319
6. Brake M (2012) An analytical elastic-perfectly plastic contact model. Int J Solids Struct 49(22):3129–3141
7. Komvopoulos K, Ye N (2001) Three-dimensional contact analysis of elastic–plastic layered media with fractal surface topographies. J Tribol 123(3):632–640
8. Mo Y, Turner KT, Szlufarska I (2009) Friction laws at the nanoscale. Nature 457(7233):1116–1119
9. Barber J, Ciavarella M (2000) Contact mechanics. Int J Solids Struct 37(1):29–43
10. Akarapu S, Sharp T, Robbins MO (2011) Stiffness of contacts between rough surfaces. Phys Rev Lett 106(20):204301
11. Almqvist A, Campaná C, Prodanov N, Persson B (2011) Interfacial separation between elastic solids with randomly rough surfaces: comparison between theory and numerical techniques. J Mech Phys Solids 59(11):2355–2369

12. Hyun S, Robbins MO (2007) Elastic contact between rough surfaces: effect of roughness at large and small wavelengths. Tribol Int 40(10):1413–1422
13. Pohrt R, Popov VL, Filippov AE (2012) Normal contact stiffness of elastic solids with fractal rough surfaces for one-and three-dimensional systems. Phys Rev E 86(2):026710
14. Carbone G, Bottiglione F (2008) Asperity contact theories: do they predict linearity between contact area and load? J Mech Phys Solids 56(8):2555–2572
15. Kogut L, Komvopoulos K (2003) Electrical contact resistance theory for conductive rough surfaces. J Appl Phys 94(5):3153–3162
16. Zhai C, Hanaor D, Proust G, Gan Y (2015) Stress-dependent electrical contact resistance at fractal rough surfaces. J Eng Mech: B4015001. doi:10.1061/(ASCE)EM.1943-7889.0000967
17. Campana C, Persson B, Müser M (2011) Transverse and normal interfacial stiffness of solids with randomly rough surfaces. J Phys Condens Matter 23(8):085001
18. Pohrt R, Popov VL (2013) Contact stiffness of randomly rough surfaces. Sci Rep 3:3293
19. Pohrt R, Popov VL (2012) Normal contact stiffness of elastic solids with fractal rough surfaces. Phys Rev Lett 108(10):104301
20. Yan W, Komvopoulos K (1998) Contact analysis of elastic–plastic fractal surfaces. J Appl Phys 84(7):3617–3624
21. Jiang S, Zheng Y, Zhu H (2010) A contact stiffness model of machined plane joint based on fractal theory. J Tribol 132(1):011401
22. Buzio R, Boragno C, Biscarini F, De Mongeot FB, Valbusa U (2003) The contact mechanics of fractal surfaces. Nat Mater 2(4): 233–236
23. Stifter T, Marti O, Bhushan B (2000) Theoretical investigation of the distance dependence of capillary and van der Waals forces in scanning force microscopy. Phys Rev B 62(20):13667
24. Putman CA, Igarashi M, Kaneko R (1995) Single-asperity friction in friction force microscopy: the composite-tip model. Appl Phys Lett 66(23):3221–3223
25. Mulvihill D, Brunskill H, Kartal M, Dwyer-Joyce R, Nowell D (2013) A comparison of contact stiffness measurements obtained by the digital image correlation and ultrasound techniques. Exp Mech 53(7):1245–1263
26. Lorenz B, Persson B (2009) Interfacial separation between elastic solids with randomly rough surfaces: comparison of experiment with theory. J Phys Condens Matter 21(1):015003
27. Hanaor D, Einav I, Gan Y (2013) Effects of surface structure deformation on static friction at fractal interfaces. Géotech Lett 3(2): 52–58
28. Chandrasekar S, Eriten M, Polycarpou A (2013) An improved model of asperity interaction in normal contact of rough surfaces. J Appl Mech 80(1):011025
29. Hanaor DA, Gan Y, Einav I (2015) Contact mechanics of fractal surfaces by spline assisted discretisation. Int J Solids Struct 59:121–131
30. Shankar S, Mayuram M (2008) Effect of strain hardening in elastic–plastic transition behavior in a hemisphere in contact with a rigid flat. Int J Solids Struct 45(10):3009–3020
31. Daphalapurkar N, Wang F, Fu B, Lu H, Komanduri R (2011) Determination of mechanical properties of sand grains by nanoindentation. Exp Mech 51(5):719–728
32. Ladani L, Harvey E, Choudhury S, Taylor C (2013) Effect of varying test parameters on elastic–plastic properties extracted by nanoindentation tests. Exp Mech 53(8):1299–1309
33. Persson B, Albohr O, Tartaglino U, Volokitin A, Tosatti E (2005) On the nature of surface roughness with application to contact mechanics, sealing, rubber friction and adhesion. J Phys Condens Matter 17(1):R1
34. Thomas T (1998) Trends in surface roughness. Int J Mach Tools Manuf 38(5):405–411
35. Go J-Y, Pyun S-I (2006) Fractal approach to rough surfaces and interfaces in electrochemistry. Modern Aspects of Electrochemistry. Springer, US, pp 167–229
36. Ciavarella M, Demelio G, Barber J, Jang YH (2000) Linear elastic contact of the Weierstrass profile. Proc R Soc Lond Ser A Math Phys Sci 456(1994):387–405
37. Dubuc B, Zucker S, Tricot C, Quiniou J, Wehbi D (1989) Evaluating the fractal dimension of surfaces. Proc R Soc Lond Ser A Math Phys Sci 425(1868):113–127
38. De Santis A, Fedi M, Quarta T (1997) A revisitation of the triangular prism surface area method for estimating the fractal dimension of fractal surfaces. Ann Geophys 40(4):811–821
39. Lu K, Lu J (2004) Nanostructured surface layer on metallic materials induced by surface mechanical attrition treatment. Mater Sci Eng A 375:38–45
40. Roland T, Retraint D, Lu K, Lu J (2007) Enhanced mechanical behavior of a nanocrystallised stainless steel and its thermal stability. Mater Sci Eng A 445:281–288
41. Proust G, Retraint D, Chemkhi M, Roos A, Demangel C (2015) Electron backscatter diffraction and transmission Kikuchi diffraction analysis of an austenitic stainless steel subjected to surface mechanical attrition treatment and plasma nitriding. Microsc Microanal 21(04):919–926
42. Liu Y, Jin B, Lu J (2015) Mechanical properties and thermal stability of nanocrystallized pure aluminum produced by surface mechanical attrition treatment. Mater Sci Eng A 636:446–451
43. Mandelbrot BB, Passoja DE, Paullay AJ (1984) Fractal character of fracture surfaces of metals. Nature 308:5961
44. Douketis C, Wang Z, Haslett TL, Moskovits M (1995) Fractal character of cold-deposited silver films determined by low-temperature scanning tunneling microscopy. Phys Rev B 51(16):11022
45. Zahn W, Zösch A (1999) The dependence of fractal dimension on measuring conditions of scanning probe microscopy. Fresenius J Anal Chem 365(1–3):168–172
46. Kim J-Y, Baltazar A, Rokhlin S (2004) Ultrasonic assessment of rough surface contact between solids from elastoplastic loading–unloading hysteresis cycle. J Mech Phys Solids 52(8):1911–1934
47. Pei L, Hyun S, Molinari J, Robbins MO (2005) Finite element modeling of elasto-plastic contact between rough surfaces. J Mech Phys Solids 53(11):2385–2409
48. Kadin Y, Kligerman Y, Etsion I (2006) Unloading an elastic–plastic contact of rough surfaces. J Mech Phys Solids 54(12):2652–2674
49. Oliver WC, Pharr GM (1992) An improved technique for determining hardness and elastic modulus using load and displacement sensing indentation experiments. J Mater Res 7(06):1564–1583
50. Oliver WC, Pharr GM (2004) Measurement of hardness and elastic modulus by instrumented indentation: advances in understanding and refinements to methodology. J Mater Res 19(01):3–20
51. Etsion I, Kligerman Y, Kadin Y (2005) Unloading of an elastic–plastic loaded spherical contact. Int J Solids Struct 42(13):3716–3729
52. Cheng C-M, Cheng Y-T (1997) On the initial unloading slope in indentation of elastic–plastic solids by an indenter with an axisymmetric smooth profile. Appl Phys Lett 71(18):2623–2625
53. Bolshakov A, Pharr G (1998) Influences of pileup on the measurement of mechanical properties by load and depth sensing indentation techniques. J Mater Res 13(04):1049–1058
54. Restagno F, Crassous J, Cottin-Bizonne C, Charlaix E (2002) Adhesion between weakly rough beads. Phys Rev E 65(4):042301
55. Kim J, Ryba E (2001) The effect of polyol OH number on the bond strength of rigid polyurethane on an aluminum substrate. J Adhes Sci Technol 15(14):1747–1762
56. Northen MT, Turner KL (2005) A batch fabricated biomimetic dry adhesive. Nanotechnology 16(8):1159
57. Oh H-J, Jang K-W, Chi C-S (1999) Impedance characteristics of oxide layers on aluminium. Bull Kor Chem Soc 20(11):1341

58. Campbell T, Kalia RK, Nakano A, Vashishta P, Ogata S, Rodgers S (1999) Dynamics of oxidation of aluminum nanoclusters using variable charge molecular-dynamics simulations on parallel computers. Phys Rev Lett 82(24):4866

59. Putignano C, Afferrante L, Carbone G, Demelio G (2012) The influence of the statistical properties of self-affine surfaces in elastic contacts: a numerical investigation. J Mech Phys Solids 60(5):973–982